

Targeted Single-Cell Therapeutics with Magnetic Tubular Micromotor by One-Step Exposure of Structured Femtosecond Optical Vortices

Liang Yang, Xiaoxiao Chen, Li Wang, Zhijiang Hu, Chen Xin, Marc Hippler, Wulin Zhu, Yanlei Hu,* Jiawen Li, Yucai Wang, Li Zhang, Dong Wu,* and Jiaru Chu

Selective manipulation of specific single cells for therapeutics is important and highly desirable in biomedical research. As a simple and maneuverable tool, tubular micromotors have displayed appealing applications in encapsulation and transportation of cells. However, so far there are no reports on the simultaneous transportation of target single cells and the drugs with microtubes in a custom arrayed environment for targeted therapeutics. Moreover, fabrication of microtubes with 3D features in a reproducible and single-step fashion, while, endowing them with the ability of remote control, remains challenging. In this study, a novel method for one-step fabrication of magnetic 3D tubular micromotors by single exposure of structured optical vortices in a magnetic photoresist is presented. The size and geometry of fabricated microtubes are flexibly controlled in three dimensions. Precise propelling of the tubular micromotors and precise capture, targeted delivery, and release of SiO₂ micro-particles are realized. Finally, as a proof-of-concept demonstration, in situ observation of the development of doxorubicin in Hela cells for therapeutic study is performed by targeted delivery of single cells and drug particles. The technology is simple and stable, which has promising applications in targeted cell therapy, drug screening, single cell studies, and other biomedical areas.

trends from biological systems. However, cell heterogeneity has been discovered to be widespread in biological processes. Hence, single cell analysis technology to resolve and make sense of this confounding heterogeneity is extremely important and highly desirable in biomedical research.^[1] In particular, in situ effects within the cell and cell's microenvironment under drug or surgical treatment is critical for understanding cell's physiological and biochemical responses, which has promising applications in drug screening,^[2,3] targeted cell treatment,^[4-7] and specialized single cell research.^[8-11] In drug screening, the point casting of drugs to specific cells for the study of cellular process that progress over time has significant advantages on resolving cell heterogeneity compared with statistical analysis of cell groups.^[2,12] For targeted cell treatment, flexible and controllable delivery of drugs to specific diseased cells and to many hard-

1. Introduction

Much of modern biological practice is designed on the basis of extracting correlations and associated statistical

to-reach tissue locations allows doctors and researchers to treat and study specific single cells more precisely and non-invasively compared with conventional surgery.^[7,9] Moreover, for drug screening and cell treatment research, it is more


Dr. L. Yang, X. Chen, Z. Hu, C. Xin, W. Zhu, Prof. Y. Hu, Prof. J. Li, Prof. D. Wu, Prof. J. Chu
Hefei National Laboratory for Physical Sciences at the Microscale
Key Laboratory of Precision Scientific Instrumentation of Anhui Higher Education Institutes
CAS Key Laboratory of Mechanical Behavior and Design of Materials
Department of Precision Machinery and Precision Instrumentation
University of Science and Technology of China
Hefei 230026, China
E-mail: huyl@ustc.edu.cn; dongwu@ustc.edu.cn

Dr. L. Yang
Institute of Nanotechnology
Karlsruhe Institute of Technology (KIT)
Hermann-von-Helmholtz-Platz 1, 76344 Eggenstein-Leopoldshafen
Germany

L. Wang, Prof. Y. Wang
The CAS Key Laboratory of Innate Immunity and Chronic Disease
School of Life Sciences and Medical Center
University of Science and Technology of China
Hefei 230027, China

M. Hippler
Institute of Applied Physics
Karlsruhe Institute of Technology (KIT)
Wolfgang-Gaede-Str. 1, 76131 Karlsruhe, Germany

Prof. L. Zhang
Department of Mechanical and Automation Engineering
The Chinese University of Hong Kong
Shatin NT, Hong Kong SAR 999077, China

 The ORCID identification number(s) for the author(s) of this article can be found under <https://doi.org/10.1002/adfm.201905745>.

DOI: 10.1002/adfm.201905745

efficient and meaningful to perform cells and drugs transportation, culturing, and analysis within an arrayed environment, which is meanwhile challenging. All these require a precise and controllable tool for the simultaneous handling of single cell and drug in custom environment and in large population.

Fuel-free artificial micromotors powered by external stimuli (e.g., magnetic, light, ultrasonic, or electric fields) has gained considerable interest in biomedical research owing to their robust miniaturized structure with functional capabilities.^[13] Magnetic propulsion is an effective way for fuel-free actuation of micromotors,^[14] as magnetic fields at low strengths are harmless to cells or tissues and can be remotely controlled without requirement of transparency or conductivity. Recently, various magnetically actuated functional micromachines, e.g., bimetal microrods,^[15] Janus microsphere,^[16] helical microwires,^[17] and so on, have been prepared. Among these diverse synthetic micromachines, tubular micromotor is one of the most simple, maneuverable, and loadable microstructure, which has displayed a controllable directionality of movement and appealing applications in the encapsulation, transportation, and release of various cargoes. Besides, microtube has played a variety of roles in structural and mechanical elements,^[18] fluid channels,^[19] containers,^[20,21] sensors,^[8,22] and lab-in-tube systems.^[9,10,23] These further increase the versatility of microtubes and expand the promising applications in microcargo delivery, cell culturing and sensing, and targeted treatment. However, present works only reported the transportation of cells^[24] or drug-carriers,^[6,20,25] or digging of cells^[7] as well as tissues^[26] with microtubes. So far there are no reports on the aspect that both the target single cells and the drug-carriers are simultaneously transported for targeted therapeutics.

A number of methods, including roll-up nanotechnology,^[7,27] deposition using porous templates,^[28] and electrospinning^[29] have been developed for the fabrication of tubular micromotors. Deposition by porous templates offers a relatively low-cost method for preparing microtubes composed of various materials such as polymers, metals, semiconductors, and carbons.^[30] The drawback of this method lies in that the geometry and sizes of microtubes is decided by the geometry of template pores. The self-assembling by roll-up nanotechnology is versatile in design, by enabling microtube to be fabricated with almost any type of inorganic materials. However, the complex fabrication procedures lead to high costs and limited control of microtube geometry. Electrospinning is an efficient and low-cost method to generate hollow polymer microtubes, and versatile in decorating the inner and outer walls with functional derivatives and metal nanoparticles. However, it suffers from disadvantages like random sizes of microtube (length, thickness, inner and outer diameter) in some range, and uncontrollable geometry of microtube (fixed circular straight hollow microtube). In fact, the geometric shape of microtubes need to be designable according to specific applications.^[31] The directionality,^[5] motility,^[32] and loading capability^[33] also raise high requirement on the designability and reproducibility of microtubes. Direct laser writing (DLW) is a versatile technique for precise fabrication of complex polymer structures in micro- and nanoscale with high

resolution.^[34] Nevertheless, the time-consuming voxel-by-voxel and layer-by-layer fashion of fabrication greatly hinders lithography throughput. Besides, for magnetism of fabricated photoresist microtubes, further process like physical deposition is required. Consequently, a simple 3D lithography technique for microtube fabrication in a reproducible and single-step fashion, which allows for high-throughput and good flexibility is highly demanded.

In this study, we present a novel method for one-step synthesis of 3D magnetic tubular micromotors with single exposure of structured femtosecond optical vortices generated by spatial light modulation. The generation, propagation and tight focusing property of the femtosecond optical vortices is systematically studied. By modulation of the optical vortices parameters, the size and geometry of the fabricated microtubes are flexibly controlled. Moreover, remote controllability and precise motion of the microtubes are realized by actuation with an external magnetic field. On this basis, the capability of these microtubes in capture, targeted delivery, and release of SiO₂ microparticles is demonstrated. Furthermore, therapeutic observation of doxorubicin treatment effect on single cell is verified by targeted delivery of HeLa cells and doxorubicin drug particles into a custom 2D microwell array. These investigations demonstrate the feasibility of these tubular micromotors as a functional tool in the manipulation of single cell and drug particle (**Figure 1a**), which has promising application in drug screening, targeted treatment, and single cell research.

2. Propagation and Focusing of Femtosecond Optical Vortex

A femtosecond laser direct writing system combined with a spatial light modulator (SLM) is used for fabrication of microtubes via a single exposure (**Figure 1b**). The femtosecond laser beam is modulated into optical vortex by pre-designed computer-generated holograms (CGHs) loaded on the SLM. The optical vortex is then rescaled by a 4f system and focused by an objective into the photoresist. The CGH is composed of two parts: spiral phase plate (SPP) and blazed grating (BG), as shown in the inset of **Figure 1b**. The SPP generates the designed optical vortex with specific intensity distribution, while the BG is an important part to separate the generated optical vortex from the zeroth-order light, which is due to the pixelation effect of the SLM. A biconical focus pattern is obtained at the focal region of the objective and is used for 3D biconical microtubes fabrication by single exposure (inset of **Figure 1b**).

To provide deeper insights into the geometry of fabricated microtubes, it is crucial to investigate the generation, propagation, and focusing property of optical vortex. A femtosecond optical vortex is generated by imprinting a vortex phase factor onto the incident Gaussian beam.^[35] The phase distribution of the CGH loaded on SLM can be expressed as

$$\text{Phase}(x, y) = l[\varphi_1 + \alpha \sin(m\varphi_1 + \beta)] + 2\pi x/\Delta \quad (1)$$

where $\text{Phase}(x, y)$ indicates the phase distribution in Cartesian coordinate, $\varphi_1 = \arctan(y/x)$, topological charge l determines

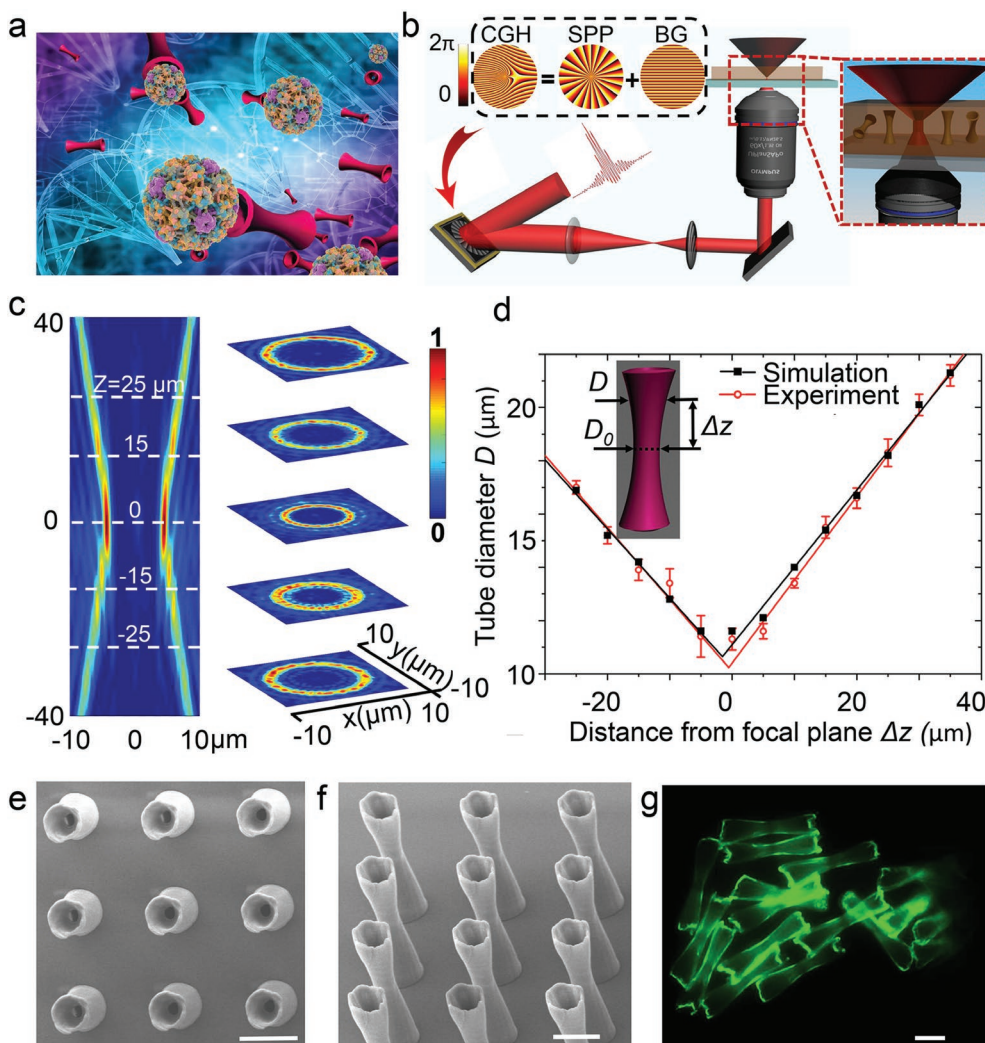


Figure 1. One step synthesis of 3D biconical microtubes with single exposure of femtosecond optical vortex. a) Scheme of promising applications of tubular microstructures as a functional tool in the manipulation of single cells and drug particles. b) Experimental setup for single exposure fabrication of microtubes. Optical vortex is generated by loading computer generated holograms onto an SLM and then focused into the resist with an objective. 3D bicone focal pattern is generated and microtubes can be fabricated by single exposure of this 3D focal pattern. The inset in the upleft corner shows that CGH is composed of a vortex phase plate and a blazed grating. The inset in the upright corner is partial enlargement at the focal region. c) Calculated light intensity distribution at the focal region in the propagation direction and at planes of -25 , -15 , 0 , 15 , and 25 μm from the focal plane, respectively. d) Experimentally measured and calculated microtube diameter at different distances from the central focal plane. The diameter is measured at five positions along circumference. e) SEM of microtubes with top and f) 45° view. g) Monodisperse microtubes in DI water after being swept down from the substrate. The scale bars are all 20 μm in (e)–(g).

the local radius of maximum intensity at angle φ_1 , α controls the depth of modulation, m produces an m -fold symmetric pattern, β determines the orientation of the pattern, and Δ represents the period of the BG. The electric field of the femtosecond optical vortex at a distance z behind SLM is derived from Fresnel diffraction theory

$$E(\rho, \theta, z) = -\frac{\exp(ikz)}{ikz} \exp\left(\frac{ik\rho^2}{2z}\right) \int_0^R \int_0^{2\pi} \text{Phase}(r, \varphi) \exp\left(\frac{ikr^2}{2z}\right) \exp\left[\frac{-ikr\rho \cos(\theta - \varphi)}{z}\right] 2\pi r dr d\varphi \quad (2)$$

Here ρ and θ are polar coordinates in the observation plane, $r = (x^2 + y^2)^{1/2}$ is the polar radius, and R is the radius of the hologram. The intensity distribution at different positions in the optical path is calculated (Figure S1, Supporting Information). The optical vortex has circular intensity distribution with a dark center in radial direction.

The geometry of the fabricated microtubes is directly related to the focal pattern. Thus, it is crucial to investigate the intensity distribution property of optical vortex in the focal region. In this study, Debye vectorial diffraction theory is adopted to describe the three orthogonal field components E_x , E_y , and E_z , respectively. Thus, the optical intensities at the focal are derived as^[36]

$$E_2(x_2, y_2, z_2) = -\frac{iC}{\lambda} \int_0^\eta \int_0^{2\pi} \sin \theta_2 E(\theta_2, \varphi_2, z_{\text{obj}}) \sqrt{\cos \theta_2} \{ [1 + (\cos \theta_2 - 1) \cos^2 \varphi_2] i + [(\cos \theta_2 - 1) \cos \varphi_2 \sin \varphi_2] j - (\sin \theta_2 \cos \varphi_2) k \} \exp[ikn_{\text{diff}}(z_2 \cos \theta_2 + x_2 \sin \theta_2 \cos \varphi_2 + y_2 \sin \theta_2 \sin \varphi_2)] d\theta_2 d\varphi_2 \quad (3)$$

where $E(\theta_2, \varphi_2, z_{\text{obj}})$ is the intensity distribution at the entrance pupil of objective derived from Equation (2), $k = 2\pi/\lambda$ is the wave number of incident light, θ_2 represents the focusing angle of objective lens, and φ_2 is the azimuthal angle of object plane. η is the maximum focusing angle of the objective lens and can be calculated according to formula: $\eta = \arcsin(\text{NA}/n)$, where n is the refractive index of immersion medium and NA is the numerical aperture of objective lens. With Equation (3), the simulated intensity distributions of a focused optical vortex ($l = 16$, $m = 0$, and $\alpha = 0$) along the propagation direction (Figure 1c, left) and at the transversal direction (Figure 1c, right) are obtained with numerical integration. The focal pattern exhibits a sand-clock intensity distribution and diverges along the propagation direction (Figure 1d).

3. One Step Synthesis of 3D Biconical Microtubes with Femtosecond Optical Vortex

By single exposure of focused optical vortex (Figure 1c), highly curved 3D microtube is fabricated by two-photon polymerization (Figure S2, Supporting Information). Figure 1e–g shows SEM images of the polymerized microtubes on glass substrates and monodisperse microtubes dispersed in deionized (DI) water after they being swept down from the substrate, with a typical height of 75 μm , minimum central diameter of 11 μm , and wall thickness of 1.1 μm . The exposure time for a single microtube is 100 ms, while it increases to 60 s with conventional single spot direct laser writing method using a piezostage (Figure S3, Supporting Information). The fabrication speed is two orders of magnitude increase. We measured the tube diameter from 25 μm in front of the focal plane to 35 μm behind the focal plane with an interval of 5 μm . The measured diameters of finally polymerized microtube fit well with theoretical calculation (Figure 1d). The diameter increases approximately linearly as the distance from focal plane Δz increase. It is found both theoretically and experimentally that the optical vortex diverges with asymmetric speed on two sides of the focal plane. For a specific optical vortex, the height of polymerized microtube is related to the focal pattern itself and exposure parameters, particularly laser power and exposure duration. The fluctuant topside of the microtubes can be attributed to the nonuniformity of intensity distribution.

In most multiphoton polymerization systems, tight focus and high resolution in the axial direction is a main pursuit for precise fabrication. Thus, laser beams usually overcover the entrance pupil of objective and diverge quickly when propagating away from the focal plane. By contrast, in this study the resized laser beam is smaller than the entrance aperture of objective, which decreases the NA and elongates the focal pattern. As a result, a 3D intensity distribution with high aspect ratio is formed. Within the focus optical vortex, photoinitiator molecules are excited by two-photon absorption from the singlet ground-state

manifold into the singlet excited-state manifold. From there, they typically undergo rapid intersystem crossing into the molecule's triplet manifold. Next, radicals are generated, which initiate the polymerization process. The monomer molecules crosslink sufficiently and form a solid polymer-network. Since the photolysis rate of the initiator, which produces free-radicals, is related to the local light intensity, the tubular intensity distribution produces a gradient of effective free-radical concentration and polymerization density, ranging from a maximum near the focal plane, to a minimum of tens of micrometers away from the focal plane. As a result, the synthesized microtubes have sand-clock 3D profiles along the light propagation direction (Figure 1c,d), rather than the thin cylindrical structure. Besides, by decreasing the height of the tubular focal pattern and scanning the focal pattern along a designed 3D route, more complex 3D microtubes can be expected, despite of straight microtubes.

4. Control of Focal Pattern and Microtube Geometry

An important aspect of this microtube manufacturing method is that the geometry of 3D microtubes can be well controlled (Figure 2). As can be seen in Equation (3), the geometry of the focal pattern as well as the microtube is related to the rescaling of the 4f systems in optical path and phase factors imprinted on incident beam by CGH in Equation (1). In particular, the extent of rescaling affects the diverging speed of the focal pattern and finally the height of the polymerized microtube. When the diameter of generated optical vortex is close to the entrance pupil of objective, the focal depth can be controlled to be $\approx 5 \mu\text{m}$. Further downscaling of the diameter increases the focal depth to tens of micrometers (Figures S4 and S5, Supporting Information). As to phase factors imprinted on incidence by CGH, m produces an m -fold symmetric pattern and topological charge l determines the radius of focal pattern. By modulating m , polygonal transversal intensity distributions can be achieved (Figure 2a) and polygonal microtubes can be fabricated with single exposure (Figure 2b; Figure S6, Supporting Information). Figure 2b shows the polymerized polygonal 3D microtubes, which exhibit triangular, square, pentagonal, and hexagonal geometry as m change from 3 to 6. To show the effects of topological charge l on the microstructure fabrication, we increased l from 4 to 30, and measured waist diameter of polymerized microtube (Figure 2e; Figure S6, Supporting Information). As l changes from 4 to 30, the diameter of microtubes increases from 3.9 to 19.8 μm , which matches well with the theoretical calculations. However, the increase of diameter is limited by the optical aperture of the optical system in the experiment. For example, in our system, when l is over 30, the optical vortex cannot fully enter the objective.

In addition to 2D modulation, we are also able to control the geometry of microtubes in 3D in our microfabrication system (Figure 2c,d). In contrast to drop casting methods, the photoresist is spin-coated on the substrate with a specific height, for example, 35 μm in our experiment. We can simply control the substrate-to-objective distance to obtain a variety of 3D microtube shapes. When the center of the focal pattern is close to the bottom of the resist film, a cone-shaped focus profile is obtained and finally a cone shaped microtube is realized (first line of Figure 2c,d). As the focus ascends, the microtube

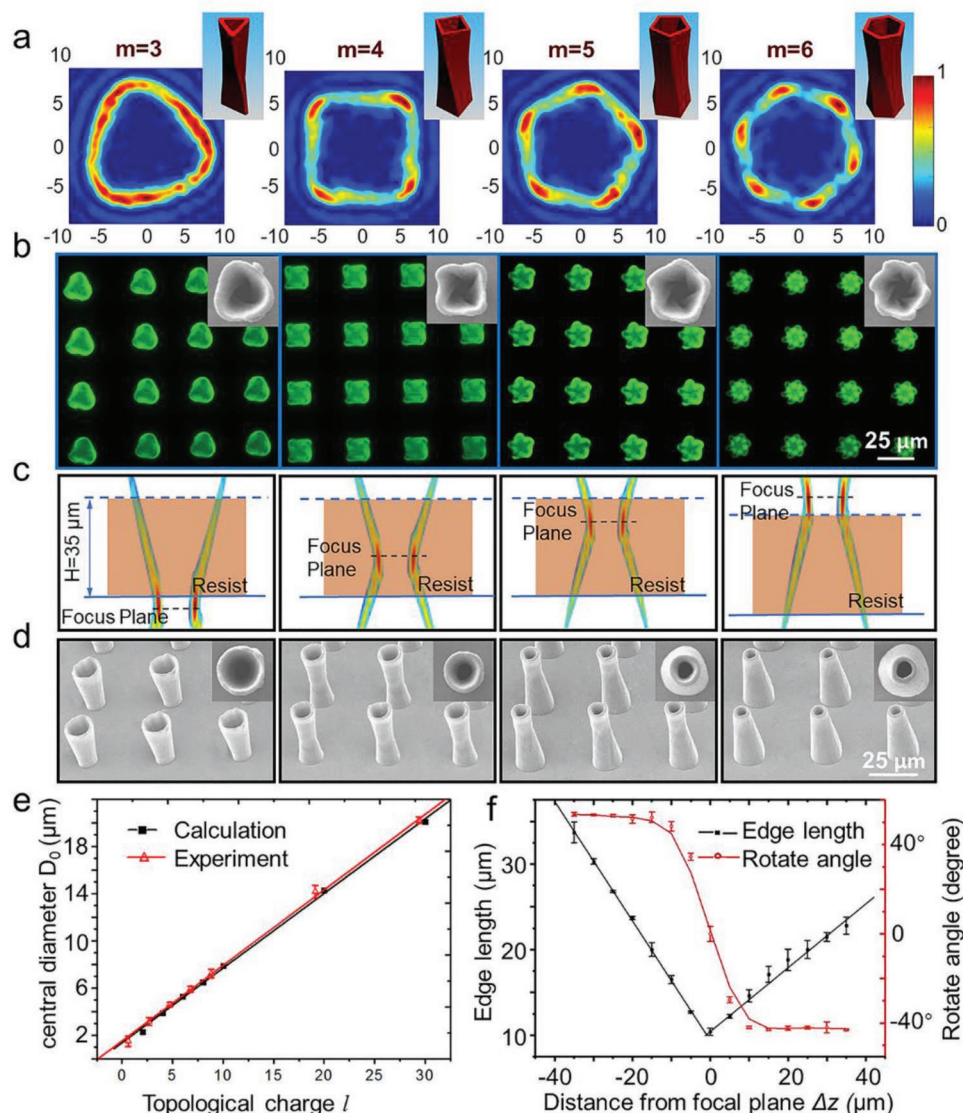


Figure 2. Control of the microtube geometry in 2D and 3D. a) By modulating phase factor m of optical vortex, polygonal transversal intensity distribution can be achieved. Besides, the focal pattern has chirality and rotates as it propagates, due to the spiral phase distribution. b) Fluorescence image and enlarged SEM images of polymerized polygonal 3D microtubes, which exhibit triangular, square, pentagonal, and hexagonal geometry from left to right as m change from 3 to 6. c) Schematic diagram of focal plane position relative to the resist height in each case. d) Highly uniform 3D microtubes of different shapes fabricated in 35 μm thick resist film, according to the focusing depth in (c). e) The waist diameter of microtube increase with the topological charge l of optical vortex. The diameters are measured at five positions along circumference. f) Measured edge length and rotation angle of triangle microtube fabricated by optical vortex with $l = 16, m = 3$.

exhibits a structure with two end lobes and a narrow central region, which well represents the focal pattern in the resist film. By moving the focal pattern in the resist, we can control the size of the two lobes of microtube and synthesize a variety of shapes (Figure 2d). To control the shapes in 3D, the resist thickness should be thinner than the height of focus.

Besides, due to the instinct spiral phase distribution, the focal pattern rotates as it propagates. So, in fact, the polymerized structures possess a specific chirality, which is related to the topological charge of optical vortex. For circular microtubes, the chirality is not obvious. But, for polygonal microtube, a rotation of the microtube along the propagation direction is found (Figure S7, Supporting Information). Figure 2f shows the variation of edge

length and rotate angle of a triangular microtube ($l = 16, m = 3$) at a distance of 35 μm in front of the focus center to 35 μm behind the central focal plane. The edge length changes asymmetrically from 33.7 μm to a minimum of 10.4 μm and then diverges to 22.8 μm , while it rotates from 54° to -43°. This chirality can facilitate the microtubes with some advanced propelling characters, for example, when propelled with rotating magnetic field.

5. Propelling and Steering of Tubular Micromotors

Photochemical materials usually used in DLW including positive and negative photoresists, hydrogels, liquid crystalline elastomers,

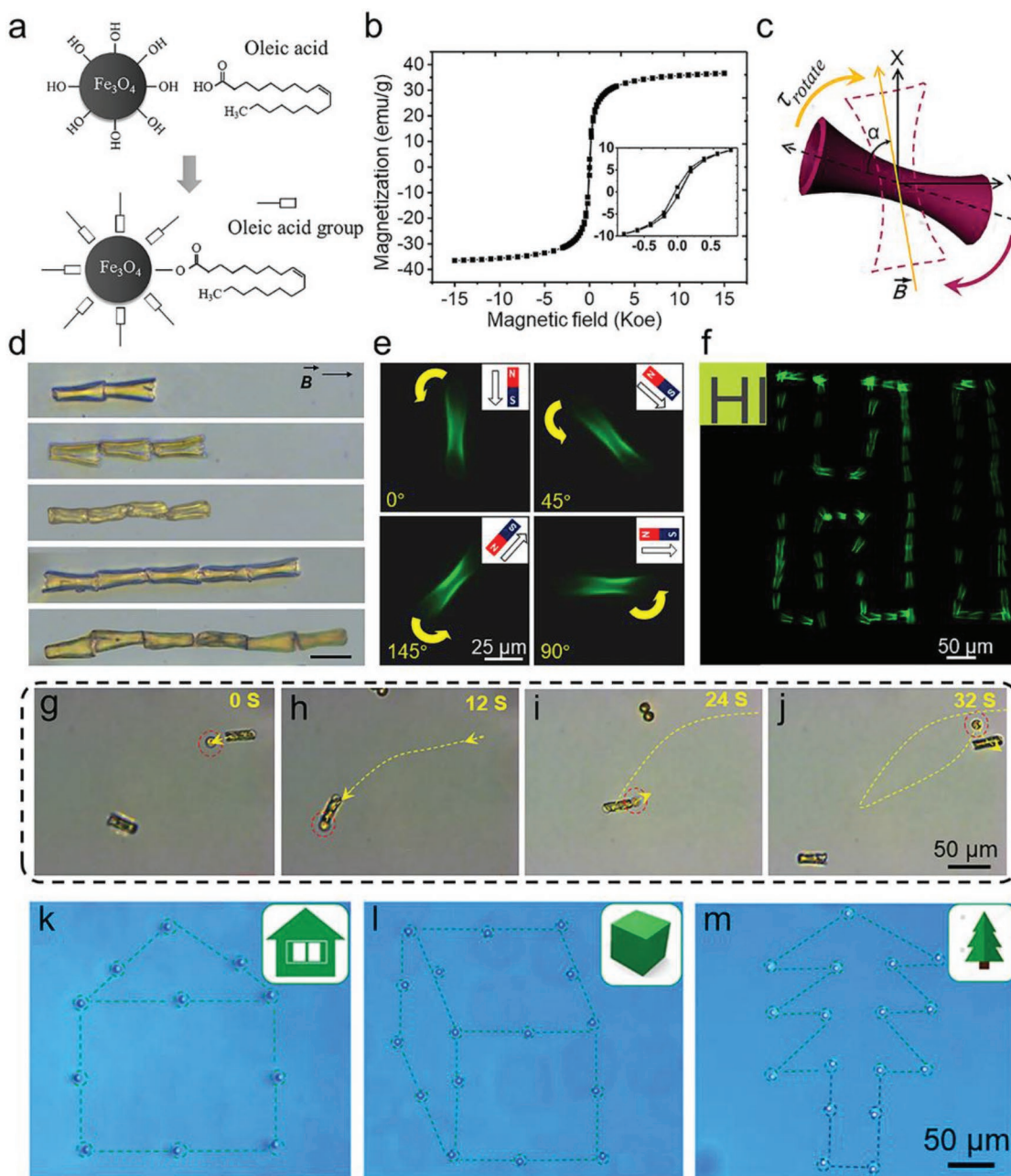


Figure 3. Propelling and steering of microtubes with external magnetic field and targeted delivery of microcargoes. a) Fe_3O_4 powder is surface-modified with oleic acid and finally dissolved in photoresist to facilitate polymerized microtubes with magnetism. b) Mass magnetization curve of magnetic microtube measured with VSM, which indicates the superparamagnetism of the magnetic microtubes. c) A magnetic torque is exerted on the microtube if there is an angle between the microtube axis and magnetic direction, which induces a rotational motion of the microtube to align along the magnetic field. d) Optical images of the linearly self-assembled magnetic microtubes in the presence of static external magnetic field. The scale bar is 12.5 μm . e) Images by fluorescence microscopy show the microtube rotation with the rotation of an external magnetic field. f) Time-lapse images show the motion of microtubes. Under the propelling and guiding of external magnetic field, a specific route of pattern “HI” is realized. g–j) Time-lapse images of delivery procedures from (g) approaching and capture, to (h) transportation, (i) changing direction and moving backward, and (j) detaching from microparticle by retreat and thus release from the front opening. k–m) House, cubic, and Christmas tree patterns composed by precisely delivered SiO_2 microparticles.

and metal salt solutions can all be used with this technique. To achieve the ability to manipulate the microtubes, Fe_3O_4 magnetic nanoparticles are surface-modified with oleic acid (Figure 3a) and mixed with commercial photoresist SZ2080 (see the Experimental Section and Figure S8, Supporting Information).

The combination of previously discussed microtube fabrication method and the use of a magnetic resist allows us to fabricate 3D microtubes with elaborate features and remote controllability by an external magnetic field. As seen from vibrating sample ferromagnetometry (VSM, Figure 3b), remanence and coercivity

could hardly be observed, indicating the superparamagnetism of the magnetic microtubes, which is highly desired for movement manipulation. For magnetic control, a droplet of DI water containing microtubes is drop casted on a cover glass, which is placed under a microscope. A permanent ferromagnet is used for remote control, which applies a magnetic torque and force on the magnetized microtube. The magnetic torque induces a rotational motion of the microtube to align along the magnetic field (Figure 3c), and the magnetic force, which is related with the magnetic field gradient, leads to the propelling of microtube.

In the presence of a static external magnetic field, the magnetic microtubes acquire dipole moments and long-range dipolar interactions. The resulting attractive interactions between the microtubes parallel to the field direction cause them to form long chains. Figure 3d shows optical images of the self-assembled magnetic microtubes. With a dynamic external magnetic field, the microtubes can be controlled to rotate and move by magnetic torque and force (Video S1 and Figure S9, Supporting Information). Figure 3e shows that the microtubes rotate sensitively and rapidly with the rotating of external magnetic field. Besides rotating, the motion of microtubes can also be well controlled by rotating and dragging of external magnetic field (Video S1, Supporting Information). Figure 3f depicts the superposition of the images of microtube locations, which shows that the microtube is manipulated to travel along a specific route of “HI”. The average swimming speeds of microtubes are 11.1–12.0 $\mu\text{m s}^{-1}$ in Video S1 (Supporting Information) and Figure 3f. 3D motion and obstacle-surmounting can also be realized by 3D propelling with external magnetic field (Figure S10, Supporting Information). In contrast to microstructures driven by light or by chemical reactions, where the motions are random or need to be manipulated individually, a group of microtubes can be manipulated synchronously by magnetic field (Figure S11, Supporting Information). It should be noted that the motion of microtube is heavily affected by external magnetic field. Besides, the microtube manipulation is in a liquid environment, where a low Reynolds number is dominated and Brownian motion becomes significant at small length scales. The viscous forces, Brownian motion, and frictions between microtube and substrates all affect the motional regulation.

6. Targeted Delivery of Cargoes with Magnetic Propelled Microtubes

More importantly, biocompatibility, high surface area, remote controllability, and high target capturing capacity due to the sand-clock 3D structure will provide magnetic microtubes with advantages in biomedical applications, especially in advanced tasks of targeted cargo delivery. The procedure of targeted micro-cargo delivery can be divided into three steps: approaching and capture, transporting to the targeted area, and releasing (Figure S12, Supporting Information). In this cargo delivery experiment, SiO_2 particles of 10 μm diameter are mixed with a suspension of magnetic microtubes in DI water. Figure 3g–j shows a time-lapse image of cargo transportation in DI water, captured from Video S3 of the Supporting Information. First, the microtube is controlled to swim toward the microparticle by dynamically changing its motion direction (Figure 3g). When the microparticle contacted with one end of the microtube, it slips into the microtube

due to the fluidic drag applied on the microparticle against the swimming direction and is thus confined in the tapered opening. The microparticle is then transported from the initial position to the target position. Because of the forward motion of the microtube and the lateral confinement from the tube walls, the microparticle is stably transported without being dislodged (Figure 3h). The motion direction is well controlled by rotating the microtube. Figure 3i shows that the microtube is turned around and the microparticle is transported back. Finally, by applying a magnetic field in opposite direction, the microtube swims backward, releasing the microparticle from the front opening (Figure 3j). The average swimming speed of microtube is around 13.4 $\mu\text{m s}^{-1}$ in the process of SiO_2 microparticles delivery.

The geometry of microtubes is an important factor affecting the successful capture and transportation. Biconical microtubes have unique advantage over straight microtube in the confinement and transportation of microcargo (Figure S13, Supporting Information). Straight microtubes are only suitable for transportation of particles with diameters larger than the microtube itself. Besides, the confinement of microparticle is solely governed by the fluidic drag, which means that the microparticle will detach from the microtube once it stops in an aqueous environment. By contrast, biconical microtubes can be used for microparticles with a wider range of diameters. Especially for particles with a diameter between the center waist and the opening, they are well confined in the microtube and can be omnidirectionally transported without possibility of detachment, even at motionless status. Besides, particles with various diameters can be loaded all in one microtube. Due to the flexibility in the design of the microtube geometry, micro- and nanoobjects of different sizes and shapes are expected to be effectively transported by changing the size and shape of the microtubes, respectively. With this cargo delivery method, complex patterns (Figure 3k–m) of microparticles are realized by designing the location of specific particles and point cast, which further demonstrated the capability of targeted delivery.

7. Targeted Delivery of Single Hela Cell and Doxorubicin Drug Particles for Therapeutic Observation

The ability of the microrobots to capture and transport both the target cells as well as drug-carriers is important for targeted treatment, single cell research, and drug screening. With microtubes, we can selectively capture the cells that we are interested in (e.g., pathological cells, cells in specific stage of division) and deliver it into a specific microwell for following treatment and observation. Here, we show the accurate delivery of cells and drugs, and observation of drug development as well as treatment effect in four steps, as depicted in Figure 4a. Polydimethylsiloxane (PDMS) substrates with μ -well arrays is prepared from deep silicon etching and replica molding (Figure S14, Supporting Information). The microwells are designed to have a diameter of $\approx 50 \mu\text{m}$, which is suitable for the accommodation of one Hela cell (10–30 μm in diameter) and several drug particles (5 μm in diameter), and a depth of 110 μm , to avoid cross-talk between different microwells. The nutrient medium containing Hela cells

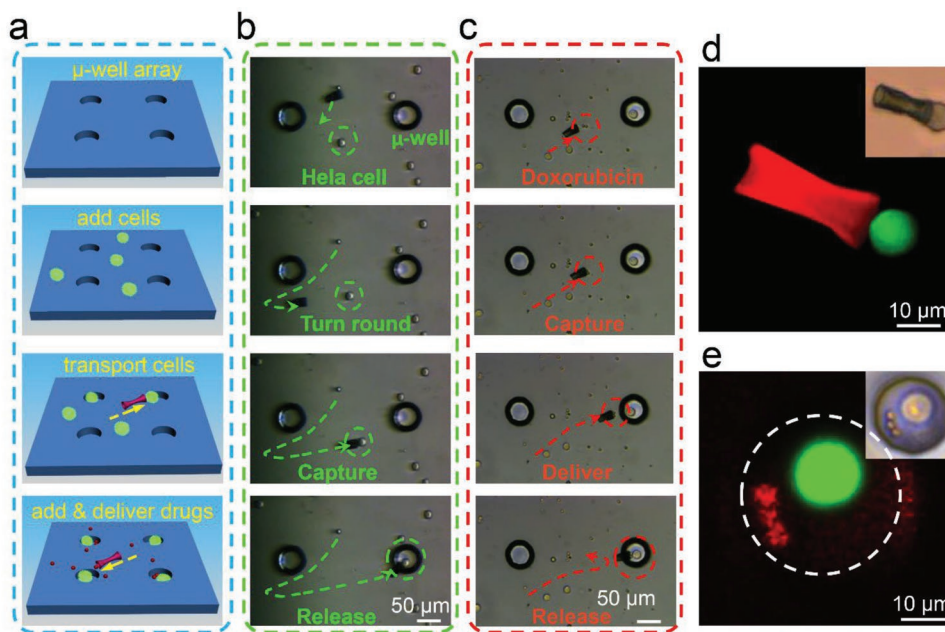


Figure 4. Targeted delivery of HeLa cells and doxorubicin particles in a custom microenvironment with μ -well arrays. a) Illustration of four experimental steps for accurate delivery of single cells and drugs: preparation of PDMS μ -well substrate, drop casting of HeLa cells, targeted delivery of HeLa cells, and adding as well as delivery of doxorubicin particles to specific HeLa cells. Optical images show the delivery process of b) HeLa cell and c) doxorubicin particles. d) Enlarged fluorescence images of cell delivery. e) Fluorescence images of HeLa cell and doxorubicin particles dwelling in a μ -well reaction center. The insets in (d) and (e) are corresponding optical images.

is blown several times and then drops casted on the PDMS substrate. It takes around 2 h for the cells to adhere on the substrate, in which period cell delivery is conducted. Next, magnetic microtubes suspended in culture medium are added for the targeted delivery of HeLa cells to specific locations, i.e., different μ -wells. Finally, particles coated with doxorubicin, which is a wide spectrum antineoplastic chemotherapy drug, is added for the successive observation of treatment effect of HeLa cells. Benefit from the advantage of biconical microtubes in handling microcargoes with wide range of diameters, HeLa cells (tens of micrometers) and doxorubicin particles (several micrometers) can be manipulated with the same kind of microtubes. Figure 4b,c is the time-lapse images of HeLa cell and drug particles delivery. As a proof-of-concept experiment, we choose the cell in the center of our observation field from all the cells as our target for further delivery and therapeutics observation. The capture, transportation and final release of the HeLa cell into a μ -well is smoothly conducted and the residence of a single HeLa cell in one μ -well is conveniently realized. The initial speed of microtube is around $27.3 \mu\text{m s}^{-1}$ and decreases to $16.6 \mu\text{m s}^{-1}$ after HeLa cell is loaded and $21.8 \mu\text{m s}^{-1}$ after drug particles are loaded. The whole process of microtube steering, cell targeting, capture and transportation, are completed in 30 s. The images in Figure 4d show the single HeLa cell capture and transportation by microtube. Figure 4e shows the final status of HeLa cell and doxorubicin particles dwelling in a μ -well. For comparison, doxorubicin particles are selectively delivered into some μ -wells with HeLa cells, while some μ -wells are only left with a single HeLa cell as a control group. Figure 5a shows a μ -well containing one HeLa cell and four doxorubicin particles. After performing the above steps, the cellular status and drug diffusion is intermittently observed by fluorescence

from the doxorubicin particles (red), over a time period of 2 h. It is obvious that the red fluorescence from the doxorubicin particles fades gradually, while the cytoplasm of HeLa cell exhibits an evident red fluorescence enhancement. The fluorescence from μ -wells cultured single cells without and with doxorubicin particles are compared in the same time scale (Figure 5b,c; Figure S15, Supporting Information). After 100 min of culture in the incubator, the green fluorescence from HeLa cells accompanied with doxorubicin particles absolutely fades out, while the control group still exhibits a strong green fluorescence, which means an effective damage of HeLa cells by doxorubicin. Quantitative analysis indicates a 98% decay of fluorescence intensities of single cells with doxorubicin particles (Figure 5e), while there is only 13.5% fluorescence decay of the control group (Figure 5d), which further demonstrated the targeted treatment of HeLa cells. Such geometry-controllable microtube, coupled with remote propelling property, facilitates the microtube robot with “on-the-spot” therapeutic action, adds a completely new and unique therapeutics capability to micromachine platforms.

In therapy, a precise and efficient method for one-step synthesis of 3D magnetic tubular micromotor is reported. 3D biconical tubular micromotors are rapidly fabricated by single exposure of ≈ 100 ms with structured femtosecond optical vortices. Compared with conventional tubular microstructure fabrication methods, this method allows for 2D and 3D control of microtube geometry, fast and high-throughput fabrication, and has sub-micrometer resolution as well as high uniformity, while surpassing limitations such as complex processing procedures, and contaminations from processing chemicals. The method has disadvantages in costs and requirements of specific equipment, and simplified fabrication setup for high throughput production needs to be further studied.

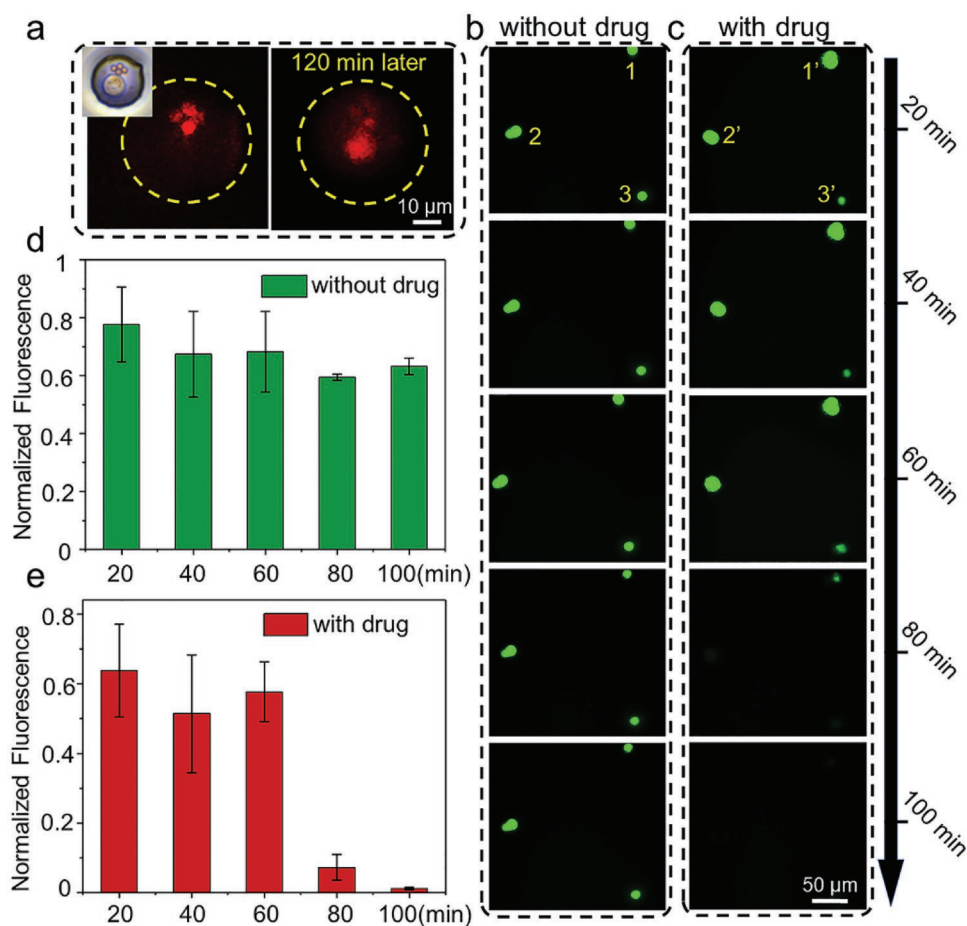


Figure 5. In situ observation of the development of doxorubicin in targeted HeLa cells and the treatment effect. a) A μ -well reaction center containing one HeLa cell and four doxorubicin particles. Inset is the optical image of HeLa cells and doxorubicin particles. After 2 h observation, red fluorescence from doxorubicin is significantly enhanced in the cytoplasm of HeLa cell. The comparison of fluorescence changes of single HeLa cells dwelling in μ -wells b) without and c) with doxorubicin particles in a time span of 100 min. Quantitative statistics of fluorescence intensity of HeLa cells d) without and e) with doxorubicin particles aside. The error bars represent the standard error of the measurements.

On the basis of this versatile fabrication method, propelling and steering of the prepared tubular micromotors by external magnetic field for precise motion is demonstrated. The tubular micromotors exhibit an excellent capability of microcargo capture, transportation, and release with better loading capacity compared with straight microtubes, magnetic particles or rods. Finally, single cancer cell therapeutics is realized by targeted delivery of HeLa cells and doxorubicin drug particles. This method offers a flexible, designable, and high-resolution one-step approach for manufacturing of remotely controllable tubular micromotors, which offers a versatile platform for the manipulation and further analyses of single cells, with advantages of specific cells targeting, remote controlling, and biocompatibility. One drawback is that manipulation of tubular micromotors needs specialized equipment and time-consuming operation, which still needs to be optimized.

8. Experimental Section

Magnetic Photoresist Preparation: $\text{FeCl}_3 \cdot 6\text{H}_2\text{O}$ (2.69 g, 0.1 mol) and $\text{FeCl}_2 \cdot 4\text{H}_2\text{O}$ (0.99 g, 0.05 mol) were dissolved in DI water (100 mL)

in a conical flask and stirred for 30 min to mix the mixture well. Next, ammonia water (25%, 4 mL) was poured into the mixed solution with rapid stirring. The mixture was stirred continuously at room temperature for 3 h. A magnet was used to collect magnetic Fe_3O_4 particles near the bottom of the flask. Then, these black particles were washed three times with DI water. After oleic acid was dropwise added as a surfactant, the Fe_3O_4 powder was precipitated from the water solvent due to the surface modification. Then, the powder was centrifuged and washed with DI water for three times to remove excess oleic acid absorbed on the particles. The prepared surface-modified magnetic particles were dissolved in *n*-hexane as stable dispersion. After commercially available photoresist SZ2080 was added, the mixture was ultrasonic stirred for 1 h at room temperature, giving the magnetic photoresist. The photoresist SZ2080 was a mixture of organic–inorganic monomer and 4,4'-bis(diethylamino)-benzophenone photoinitiator at 1% by weight.^[37]

Experimental Setup: A femtosecond laser direct writing system combined with spatial light modulation modules was used for producing microtubes. A Ti:sapphire laser oscillator (Chameleon vision-S, Coherent Corp.) with a central wavelength of 780 nm, repetition rate of 80 MHz, and pulse duration of 75 fs was used as the light source. After passing through a beam expander, the laser beam illuminated a reflection type liquid crystal SLM (1920 \times 1080 pixels, 256 gray levels, pixel pitch of 8 μm , Pluto NIR II, Holoeye), on which CGHs were encoded. Only the central 1080 \times 1080 pixels were used for phase modulation and the other

pixels were assigned to zero as a reflective mirror. The femtosecond optical vortex beam was generated on the 1st order behind the SLM and then condensed by two lenses, before being focused into photosensitive material with a high numerical aperture objective (60×, NA = 1.35, Olympus). Photoresist sample was anchored to a 3D nanopositioning stage (E545, Physik Instrument). The fabrication process was monitored in situ with a charge coupled device camera. The fabrication system is schematically illustrated in Figure 1b. After polymerization by the focused femtosecond optical vortex beam, the sample was developed in 1-propanol for 30 min until all of the unpolymerized parts were washed away, and then microtubes could be obtained by spontaneously evaporating the developer.

Synthesis of Doxorubicin Microparticles: SiO₂ particles (5 μm) were modified by 3-aminopropyl triethoxysilane (APTES) in toluene overnight and purified using centrifugation with toluene by washing for five times to remove free APTES. Typically, doxorubicin (16 mg, 0.031 mmol) was dissolved in 8 mL of dimethyl sulfoxide on ice. Then PEG-*b*-PHEMA_{CMA} (0.25 g, 0.024 mmol) was added to conjugate DOX. Next, the reaction mixture was stirred for 2 h and later allowed to cool back to room temperature for 4 h. SiO₂ particles (5 μm) were added in dimethyl sulfoxide followed by stirring at room temperature overnight. The mixture was purified by centrifugation for five times with dimethyl sulfoxide to remove doxorubicin and five times with PBS to suspend for next use.

Cell Culture: Hela-EGFP cells were obtained from American Type Culture Collection and cultured in a humidified atmosphere at 37 °C with 5% CO₂. The cells were cultured in normal Dulbecco's modified eagle medium (Gibco, Thermo Fisher Scientific, Grand Island, NY) supplemented with 10% fetal bovine serum (HyClone, Logan, UT) and 1% penicillin/streptomycin (Gibco, Life Technologies, Grand Island, NY). For single cell therapeutic experiment, Hela cells were detached from culture dish by trypsinization with 0.25% Trypsin-EDTA (Gibco, USA) at 37 °C for 30 s, centrifuged at 1000 rpm for 5 min. Then cells were resuspended in culture medium at a density of 2 × 10⁶ mL⁻¹ for use.

Supporting Information

Supporting Information is available from the Wiley Online Library or from the author.

Acknowledgements

This work was supported by the National Science Foundation of China (Nos. 61805230, 51675503, 51875544, 51805508, and 51805509), the Fundamental Research Funds for the Central Universities (WK2090000013, WK2090090012, WK2090090021, WK2090090024, and WK2090090025), Youth Innovation Promotion Association CAS (2017495), National Key R&D Program of China (2017YFB1104303 and 2018YFB1105400), and Foundation of Equipment Development Department (6220914010901). Thanks for the USTC Center for Micro and Nanoscale Research and Fabrication.

Conflict of Interest

The authors declare no conflict of interest.

Keywords

direct laser writing, micromotors, optical vortex, single cell analysis, spatial light modulation

Received: July 16, 2019
Revised: August 15, 2019
Published online:

- [1] a) L. Mazutis, J. Gilbert, W. L. Ung, D. A. Weitz, A. D. Griffiths, J. A. Heyman, *Nat. Protoc.* **2013**, *8*, 870; b) D. A. Lawson, N. R. Bhakta, K. Kessenbrock, K. D. Prummel, Y. Yu, K. Takai, A. Zhou, H. Eyob, S. Balakrishnan, C. Y. Wang, P. Yaswen, A. Goga, Z. Werb, *Nature* **2015**, *526*, 131.
- [2] J. R. Heath, A. Ribas, P. S. Mischel, *Nat. Rev. Drug Discovery* **2016**, *15*, 204.
- [3] M. Yu, A. Bardia, N. Aceto, F. Bersani, M. W. Madden, M. C. Donaldson, R. Desai, H. L. Zhu, V. Comaills, Z. L. Zheng, B. S. Wittner, P. Stojanov, E. Brachtel, D. Sgroi, R. Kapur, T. Shioda, D. T. Ting, S. Ramaswamy, G. Getz, A. J. Iafrate, C. Benes, M. Toner, S. Maheswaran, D. A. Haber, *Science* **2014**, *345*, 216.
- [4] J. X. Li, B. E. F. de Avila, W. Gao, L. F. Zhang, J. Wang, *Sci. Rob.* **2017**, *2*, eaam6431.
- [5] J. X. Li, I. Rozen, J. Wang, *ACS Nano* **2016**, *10*, 5619.
- [6] Z. G. Wu, Y. J. Wu, W. P. He, X. K. Lin, J. M. Sun, Q. He, *Angew. Chem., Int. Ed.* **2013**, *52*, 7000.
- [7] A. A. Solovev, W. Xi, D. H. Gracias, S. M. Harazim, C. Deneke, S. Sanchez, O. G. Schmidt, *ACS Nano* **2012**, *6*, 1751.
- [8] E. J. Smith, S. Schulze, S. Kiravittaya, Y. F. Mei, S. Sanchez, O. G. Schmidt, *Nano Lett.* **2011**, *11*, 4037.
- [9] W. Xi, C. K. Schmidt, S. Sanchez, D. H. Gracias, R. E. Carazo-Salas, S. P. Jackson, O. G. Schmidt, *Nano Lett.* **2014**, *14*, 4197.
- [10] W. Xi, C. K. Schmidt, S. Sanchez, D. H. Gracias, R. E. Carazo-Salas, R. Butler, N. Lawrence, S. P. Jackson, O. G. Schmidt, *ACS Nano* **2016**, *10*, 5835.
- [11] a) M. Hippler, E. D. Lemma, S. Bertels, E. Blasco, C. Barner-Kowollik, M. Wegener, M. Bastmeyer, *Adv. Mater.* **2019**, *31*, 1808110; b) B. Koch, S. Sanchez, C. K. Schmidt, A. Swiersy, S. P. Jackson, O. G. Schmidt, *Adv. Healthcare Mater.* **2014**, *3*, 1753.
- [12] O. Kepp, L. Galluzzi, M. Lipinski, J. Y. Yuan, G. Kroemer, *Nat. Rev. Drug Discovery* **2011**, *10*, 221.
- [13] a) T. L. Xu, W. Gao, L. P. Xu, X. J. Zhang, S. T. Wang, *Adv. Mater.* **2017**, *29*, 1603250; b) F. Wong, K. K. Dey, A. Sen, *Annu. Rev. Mater. Res.* **2016**, *46*, 407; c) H. Wang, M. Pumeria, *Chem. Rev.* **2015**, *115*, 8704; d) K. Han, C. W. Shields, N. M. Diwakar, B. Bharti, G. P. Lopez, O. D. Velev, *Sci. Adv.* **2017**, *3*, e1701108.
- [14] a) B. J. Nelson, I. K. Kaliakatsos, J. J. Abbott, *Annu. Rev. Biomed. Eng.* **2010**, *12*, 55; b) P. Fischer, A. Ghosh, *Nanoscale* **2011**, *3*, 557; c) L. Zhang, T. Petit, K. E. Peyer, B. J. Nelson, *Nanomed.: Nanotechnol., Biol., Med.* **2012**, *8*, 1074; d) S. Kim, F. M. Qiu, S. Kim, A. Ghanbari, C. Moon, L. Zhang, B. J. Nelson, H. Choi, *Adv. Mater.* **2013**, *25*, 5863.
- [15] a) W. Gao, D. Kagan, O. S. Pak, C. Clawson, S. Campuzano, E. Chuluun-Erdene, E. Shipton, E. E. Fullerton, L. F. Zhang, E. Lauga, J. Wang, *Small* **2012**, *8*, 460; b) J. X. Li, T. L. Li, T. L. Xu, M. Kiristi, W. J. Liu, Z. G. Wu, J. Wang, *Nano Lett.* **2015**, *15*, 4814; c) W. Wang, W. T. Duan, Z. X. Zhang, M. Sun, A. Sen, T. E. Mallouk, *Chem. Commun.* **2015**, *51*, 1020.
- [16] a) H. R. Jiang, N. Yoshinaga, M. Sano, *Phys. Rev. Lett.* **2010**, *105*, 268302; b) C. Maggi, F. Saglimbeni, M. Dipalo, F. De Angelis, R. Di Leonardo, *Nat. Commun.* **2015**, *6*, 7855.
- [17] a) S. Ghosh, A. Ghosh, *Sci. Robot.* **2018**, *3*, eaq0076; b) S. Tottori, L. Zhang, F. M. Qiu, K. K. Krawczyk, A. Franco-Obregon, B. J. Nelson, *Adv. Mater.* **2012**, *24*, 811; c) W. Gao, X. M. Peng, A. Pei, C. R. Kane, R. Tam, C. Hennessy, J. Wang, *Nano Lett.* **2014**, *14*, 305.
- [18] a) S. D. Gittard, A. Nguyen, K. Obata, A. Koroleva, R. J. Narayan, B. N. Chichkov, *Biomed. Opt. Express* **2011**, *2*, 3167; b) Z. L. Xiang, H. Wang, A. Pant, G. Pastorin, C. Lee, *Biomeicrofluidics* **2013**, *7*, 026502.
- [19] G. S. Huang, Y. F. Mei, F. Cavallo, S. Baunack, E. Coric, T. Gemming, F. Bertram, J. Christen, R. K. Y. Fu, P. K. Chu, O. G. Schmidt, *J. Appl. Phys.* **2009**, *105*, 016103.
- [20] J. X. Li, S. Thamphiwatana, W. J. Liu, B. E. F. de Avila, P. Angsantikul, E. Sandraz, J. X. Wang, T. L. Xu, F. Soto, V. Ramez, X. L. Wang, W. W. Gao, L. F. Zhang, J. Wang, *ACS Nano* **2016**, *10*, 9536.

- [21] F. Soto, A. Martin, S. Ibsen, M. Vaidyanathan, V. Garcia-Gradilla, Y. Levin, A. Escarpa, S. C. Esener, J. Wang, *ACS Nano* **2016**, *10*, 1522.
- [22] S. M. Harazim, V. A. B. Quinones, S. Kiravittaya, S. Sanchez, O. G. Schmidt, *Lab Chip* **2012**, *12*, 2649.
- [23] S. Sanchez, *Lab Chip* **2015**, *15*, 610.
- [24] a) S. Balasubramanian, D. Kagan, C. M. J. Hu, S. Campuzano, M. J. Lobo-Castanon, N. Lim, D. Y. Kang, M. Zimmerman, L. F. Zhang, J. Wang, *Angew. Chem., Int. Ed.* **2011**, *50*, 4161; b) S. Campuzano, J. Orozco, D. Kagan, M. Guix, W. Gao, S. Sattayasamitsathit, J. C. Claussen, A. Merkoci, J. Wang, *Nano Lett.* **2012**, *12*, 396; c) V. Magdanz, M. Guix, F. Hebenstreit, O. G. Schmidt, *Adv. Mater.* **2016**, *28*, 4084.
- [25] S. K. Srivastava, M. Medina-Sanchez, B. Koch, O. G. Schmidt, *Adv. Mater.* **2016**, *28*, 832.
- [26] G. Chatzipirpiridis, O. Ergeneman, J. Pokki, F. Ullrich, S. Fusco, J. A. Ortega, K. M. Sivaraman, B. J. Nelson, S. Pane, *Adv. Healthcare Mater.* **2015**, *4*, 209.
- [27] a) G. S. Huang, Y. F. Mei, D. J. Thurmer, E. Coric, O. G. Schmidt, *Lab Chip* **2009**, *9*, 263; b) S. Zakharchenko, E. Sperling, L. Ionov, *Biomacromolecules* **2011**, *12*, 2211.
- [28] a) C. R. Martin, *Chem. Mater.* **1996**, *8*, 1739; b) Y. Yang, Q. He, L. Duan, Y. Cui, J. B. Li, *Biomaterials* **2007**, *28*, 3083; c) J. B. Gilbert, J. S. O'Brien, H. S. Suresh, R. E. Cohen, M. F. Rubner, *Adv. Mater.* **2013**, *25*, 5948; d) W. Gao, J. Wang, *ACS Nano* **2014**, *8*, 3170.
- [29] a) Y. Yu, L. Gu, C. B. Zhu, P. A. van Aken, J. Maier, *J. Am. Chem. Soc.* **2009**, *131*, 15984; b) A. Sitt, J. Soukupova, D. Miller, D. Verdi, R. Zboril, H. Hess, J. Lahann, *Small* **2016**, *12*, 1432.
- [30] a) W. Gao, S. Sattayasamitsathit, A. Uygun, A. Pei, A. Ponedal, J. Wang, *Nanoscale* **2012**, *4*, 2447; b) R. Maria-Hormigos, B. Jurado-Sanchez, L. Vazquez, A. Escarpa, *Chem. Mater.* **2016**, *28*, 8962.
- [31] a) T. C. von Erlach, S. Bertazzo, M. A. Wozniak, C. M. Horejs, S. A. Maynard, S. Attwood, B. K. Robinson, H. Autefage, C. Kallepitis, A. D. Hernandez, C. S. Chen, S. Goldoni, M. M. Stevens, *Nat. Mater.* **2018**, *17*, 237; b) W. G. Yang, H. B. Yu, G. X. Li, F. N. Wei, Y. C. Wang, L. Q. Liu, *Lab Chip* **2017**, *17*, 4243.
- [32] Y. F. Mei, A. A. Solovev, S. Sanchez, O. G. Schmidt, *Chem. Soc. Rev.* **2011**, *40*, 2109.
- [33] X. H. Yan, Q. Zhou, J. F. Yu, T. T. Xu, Y. Deng, T. Tang, Q. Feng, L. M. Bian, Y. Zhang, A. Ferreira, L. Zhang, *Adv. Funct. Mater.* **2015**, *25*, 5333.
- [34] a) E. Stankevicius, T. Gertus, M. Rutkauskas, M. Gedvilas, G. Raciukaitis, R. Gadonas, V. Smilgevicius, M. Malinauskas, *J. Micro-mech. Microeng.* **2012**, *22*, 065022; b) W. S. Yan, M. M. Hossain, M. Gu, *Opt. Lett.* **2013**, *38*, 3177.
- [35] J. E. Curtis, D. G. Grier, *Opt. Lett.* **2003**, *28*, 872.
- [36] a) H. Lin, B. H. Jia, M. Gu, *Opt. Lett.* **2011**, *36*, 406; b) X. Hao, C. F. Kuang, Y. H. Li, X. Liu, *J. Opt.* **2012**, *14*, 045702.
- [37] A. Ovsianikov, J. Viertel, B. Chichkov, M. Oubaha, B. MacCraith, L. Sakellari, A. Giakoumaki, D. Gray, M. Vamvakaki, M. Farsari, C. Fotakis, *ACS Nano* **2008**, *2*, 2257.